Nonlinear Dyn
https://doi.org/10.1007/s11071-024-10458-5

RESEARCH

Nonlinear plane-wave expansion method for analyzing dispersion properties of piezoelectric metamaterial lattices with encapsulated resonators

Yichang Shen · Walter Lacarbonara

Received: 23 July 2024 / Accepted: 6 October 2024

Abstract Wave propagation and band gap behavior of square lattices encapsulating identical nonlinear resonators in each cell are investigated through an asymptotic treatment of the wave propagation equations. The nonlinear effects of the resonators, composed of suspended piezoelectric membranes with a central mass, are investigated through the introduction of a generalized nonlinear version derived from the plane-wave expansion (PWE) method. This method leads to nonlinear wave propagation equations and the analytical derivation of nonlinear dispersion functions using the method of multiple scales. Numerical simulations verify the validity of the analytical solutions. The proposed nonlinear PWE method is shown to overcomes the limitations of the popular approach based on the enforcement of the Floquet–Bloch theorem in the context of the cell projection method. While the latter provides the dispersion curves of the fundamental propagation mode, the nonlinear PWE delivers the nonlinear dispersion curves of all modes, offering a broader perspective into the design process for semi-adaptively programmable metamaterials aimed at controlling wave propagation.

Y. Shen (✉) · W. Lacarbonara
Department of Structural and Geotechnical Engineering, Sapienza University of Rome, 00184 Rome, Italy
e-mail: shenyichang93@163.com

W. Lacarbonara
e-mail: walter.lacarbonara@uniroma1.it

Keywords Metamaterials · Plane-wave expansion · Nonlinear local resonances · Dispersion functions · Acoustic/optical propagation modes · Method of multiple scales

1 Introduction

Metamaterial structures are attracting a great deal of attention thanks to their capability of suppressing or attenuating the propagation of elastic waves via manipulation of the stopbands. The formation of stopbands includes Bragg scattering, inertial amplification, local resonance etc, general details of the mechanisms of metamaterials can be found in few textbooks, e.g., [1,2] and review articles [3–5], to list but a few. Local resonance stopbands are the focus of the present work because they show less dependence on the periodicity of the structure, and turn out to be easily tunable through proper structural design optimizations. Studies addressing 2D periodic structures with local resonance mechanisms can be found in several previous works, see, e.g., [6–14].

Among the analytical methods for periodic structures, the well-known Plane Wave Expansion (PWE) method [15] is widely employed for dealing with wave propagation in periodic systems. In [16], the authors applied the PWE method to analyse periodic 3D metamaterials consisting of spherical inclusions in a cubic lattice, while in [17], they applied the PWE method for computing dispersion properties using Mindlin's plate

Published online: 23 October 2024

theory considering concentric circular inclusions, and the results were compared with those obtained using Kirchhoff's plate theory and full 3D models. Miranda Jr et al. [18,19] employed the PWE and extended PWE methods to theoretically investigate the flexural waves propagating in an elastic square lattice metamaterial with attached local resonators, where Kirchhoff-Love thin plate theory and Mindlin-Reissner thick plate theory were considered, respectively. Recently, a 2D metamaterial cellular system inspired by lightweight honeycombs and spider webs was proposed and investigated in [20], whereby the PWE method was employed to obtain the dispersion curves and the stopband sensitivity with respect to the design parameters, experimental results further validated the theoretical predictions and confirmed the robustness of the stopband behavior.

In the last decades, the topic has been approached by the community of nonlinear dynamicists. Herein we list a few recent papers for sake of conciseness. In [21], the authors presented and analyzed four highly nonlinear metamaterial models to illustrate the evolution of typical nonlinear band structures by employing the harmonic balance method. In [22] a movable metamaterial propelled by nonlinear elastic waves was addressed. Inspired by stopband properties, it introduced nonreciprocal crawling, behaving as a dynamic mechanical diode. In [23], the authors investigated theoretically and experimentally a metamaterial beam endowed with the nonlinear magnetic mass-beam resonators to achieve tunable band gaps. In particular, the method of multiple scales [24] has been widely employed and investigated for stopband calculations, wave propagation predictions, and vibration analysis. In [25], the authors presented a comprehensive review of recent advancements in the analysis, experimental investigation, and practical applications of wave propagation within weakly nonlinear metamaterials. In [26], the authors carried out analysis of dispersive wave propagation via the method of multiple scales in which the homogeneous solutions were considered at each order. More recently, in [27], the nonlinear tension-torsion coupling motion of Kresling origami was tackled and the method of multiple scales employed for deriving the first-order solutions for the semi-infinite system.

As the programmability (see, e.g., [28]), tunability (see, e.g., [23,29,30]) and optimality (see, e.g., [31–33]) for stopband widths in metamaterials are increasingly pursued as venues for unprecedented performance in wave cloaking in practical applications, in prior work of the present authors [34], the investigation centered on a metamaterial featuring membrane resonators aimed to create highly adjustable band gaps by manipulating the membrane modal properties through the application of voltage-induced membrane stretching/tension via the piezoelectric effect. The projection method [33,35,36], which works well for analysing frequency stopbands within the fundamental propagating mode, was applied to obtain a closed-form representation of the linear and nonlinear dispersion properties of the system. However, it is crucial to thoroughly understand all the propagating modes of the metamaterial system. To this end, here analytical and numerical studies are conducted to examine the impact of local nonlinear resonances on the nonlinear dispersion relations of the metamaterial. The PWE method is explored and implemented for metamaterials weakly coupled with nonlinear resonators, and the method of multiple scales is employed to obtain the nonlinear dispersion functions of the nonlinear coupled system.

The paper is organized as follows. After the Introduction, in Sect. 2, the modeling approach yielding the equations governing wave propagation is proposed. Section 3 discusses the PWE method applied to the nonlinear metamaterial coupled system. In Sect. 4, the linear dispersion relationships are introduced by solving the eigenvalue problem, and nonlinear dispersion relationships are obtained via the method of multiple scales. The numerical investigation and validation into the nonlinear stopbands has been made in Sect. 5. The summary with the main findings of this study is provided in Sect. 6.

2 Analytical metamaterial model

The considered metamaterial is a lattice constituted by square thin-walled cells supporting, in the midplane, suspended membranes with central masses (see Fig. 1). Such lattice was first introduced and analysed in [34]. The square frames surrounding the flexible membranes are sufficiently stiff to ensure the load-bearing capacity of the entire periodically patterned plate. Although the global modes of the infinite plate induce out-of-plane deformations of the unit cells, these deformations are small enough to neglect their influence on the local modes of the membranes, which have much higher frequencies. We will provide next an overview of the formulation of the membrane resonators together incor-

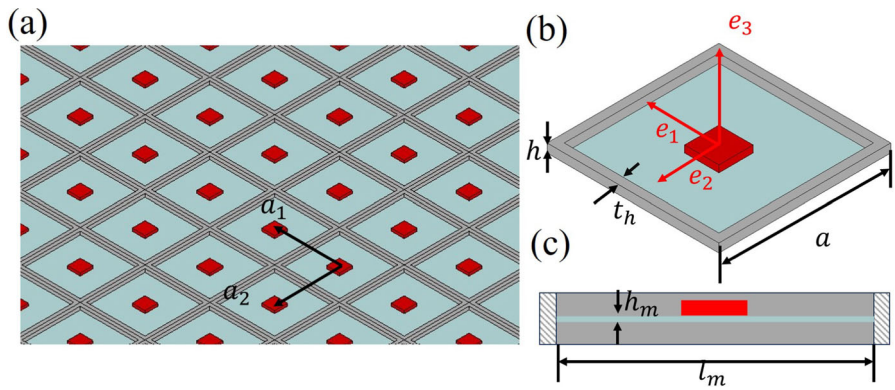

Fig. 1 **a** Schematic view of the lattice with the periodically distributed membrane-mass resonators (shown in part (**b**) with a cross-section in (**c**)). The square cell geometry with thickness h, side length a, wall width t_h. The lattice vectors are denoted by $(\mathbf{a}_1, \mathbf{a}_2)$ and the fixed frame by $(\mathbf{e}_1, \mathbf{e}_2, \mathbf{e}_3)$

porating the full model of the overall lattice with the membrane resonators.

2.1 Nonlinear membrane resonator modeling

The resonators are modelled as homogeneous isotropic piezoelectric membranes holding central lumped masses $M^{(C)}$. The nonlinear equation of motion for a membrane resonator is reduced via the Galerkin method employing the basis of membrane eigenfunctions obtained with fixed boundary conditions. The resulting reduced-order model of the membrane resonators are thus described in terms of modal mass, linear and nonlinear modal stiffness. The membrane resonators are assumed to have negligible damping. For treatment of damping, see [37]. Full details of the model formulation can be found in [34], here we merely review the main equations.

We consider initially only the mnth mode with the assumption that each mode is away from internal resonances with other membrane modes. The single-mode reduced model of the resonator, obtained by applying the Galerkin method on the cell domain, reads as [34]:

$$M_{mn}\ddot{z}_{mn}(t) + K_{mn}z_{mn}(t) + K^{(3)}_{mn}z^3_{mn}(t) = 0, \tag{1}$$

where the overdot indicates differentiation with respect to time t. The modal mass M_{mn}, the modal stiffness K_{mn}, and the nonlinear stiffness coefficient $K^{(3)}_{mn}$ are expressed as:

$$\begin{aligned} M_{mn} &= \frac{\rho_m h_m l_m^2}{4} + M^{(C)} \sin^2\left(\frac{m\pi}{2}\right)\sin^2\left(\frac{n\pi}{2}\right), \\ K_{mn} &= n^{(0)}\left(\frac{\pi}{2}\right)^2\left[m^2+n^2\right], \\ K^{(3)}_{mn} &= \frac{3E_m h_m \pi^4}{64 l_m^2}\left[m^2+n^2\right], \end{aligned} \tag{2}$$

where l_m is the characteristic length of the membrane, ρ_m is the mass density, and h_m is the membrane thickness, E_m is the Young modulus of the membrane piezoelectric polymer material. The membrane pre-stress $n^{(0)}$ can be effectively tuned by suitably changing the applied DC voltage thanks to the piezoelectricity. In our study, by adopting PVDF (PolyVinylidene DiFluoride) as piezoelectric polymer, the tension arising in the membrane due to the piezoelectric strain can be expressed as

$$n^{(0)} = E_m \int_0^{h_m} \frac{d_0 V}{h_m} dz = E_m d_0 V, \tag{3}$$

where $d_0 = 1.358 \times 10^{-11} C/N$ is the nominal coupling piezoelectric coefficient for PVDF. The pre-stress is directly proportional to the applied DC voltage V, the Young modulus E_m, and the coupling piezoelectric coefficient d_0.

The subscript mn can be substituted with a single index associated with the ordering of the modal frequencies; for example, one can set, for convenience, $M_{11} = M_1$, $M_{21} = M_2$, $M_{22} = M_3$, etc. In the next sections, we shall use only the subscript r to indicate the sequential modal number of the resonator mode according to the adopted modal ordering.

2.2 Metamaterial modeling

Figure 1 illustrates the reference configuration of the indefinitely periodic lattice, which can be modelled as an equivalent orthotropic plate depending on the selected lattice geometry. The plate reference plane is positioned in the $(\mathbf{e}_1, \mathbf{e}_2)$-plane of the fixed frame, while the positions of the equivalent membrane resonators are ruled by the lattice vectors $(\mathbf{a}_1, \mathbf{a}_2)$.

Each membrane resonator shall be interpreted and treated as a nonlinear multi-mass-spring system resulting from the multi-dof Galerkin reduction of the spatially continuous (infinite-dimensional) membrane with the attached central mass, as discussed above. Each resonator is thus equivalently represented by modal masses and modal springs positioned at lattice points $\mathbf{x}^{(ij)} = i\mathbf{a}_1 + j\mathbf{a}_2$, with i and j being integers, $\mathbf{a}_1 = (a_{11}, a_{12}) = (a, 0)$ and $\mathbf{a}_2 = (a_{21}, a_{22}) = (0, a)$ being the direct lattice vectors with a denoting the lattice parameter.

The mass density ρ^* of the equivalent, homogenized orthotropic plate model is derived from the homogenization originally proposed in [38] and the effective bending stiffness coefficients of the equivalent orthotropic plate reported in [39] are given in "Appendix A". The thin plate theory (see [40]) is employed to model the equivalent orthotropic plate with the attached resonators. The equations of motion for the coupled system represented by the orthotropic plate with the resonators can thus be expressed as

$$\begin{aligned}
&\rho^\star h \frac{\partial^2 w(\mathbf{x},t)}{\partial t^2} + \left[D_{11}^* \frac{\partial^4 w(\mathbf{x},t)}{\partial x_1^4} + 2(D_{12}^* + 2D_{66}^*) \right. \\
&\left. \frac{\partial^4 w(\mathbf{x},t)}{\partial x_1^2 \partial x_2^2} + D_{22}^* \frac{\partial^4 w(\mathbf{x},t)}{\partial x_2^4} \right] \\
&+ \sum_r \sum_{i,j} M_r^{(ij)} \left[\ddot{w}(\mathbf{x},t) + \ddot{z}_r^{(ij)}(t) \right] \\
&\delta(\mathbf{x} - \mathbf{x}^{(ij)}) = 0, \\
&M_r^{(ij)} \left[\ddot{w}(\mathbf{x}^{(ij)},t) + \ddot{z}_r^{(ij)}(t) \right] \\
&+ K_r^{(ij)} z_r^{(ij)}(t) + K_r^{(ij)(3)} (z_r^{(ij)}(t))^3 = 0, \\
&\text{with} \quad r = 1, \ldots R, \quad i, j = -\infty, \ldots, \infty,
\end{aligned} \tag{4}$$

where $\mathbf{x} = x_1\mathbf{e}_1 + x_2\mathbf{e}_2$ is the position vector for an arbitrary material point of the plate mid-surface, t is time, $w(\mathbf{x}, t)$ is the displacement of the plate at position $\mathbf{x}$ and time t, $z_r^{(ij)}$ is the modal amplitude of the rth mode of the (ij)th resonator (i.e, the resonator positioned at $\boldsymbol{x}^{(ij)}$), R is the number of retained resonators modes, h is the plate thickness, $D_{rs}^\star$ are the equivalent plate bending stiffness coefficients, and $\rho^\star$ is the density of the equivalent plate whose expressions are given in "Appendix A"; $K_r^{(ij)}$, $M_r^{(ij)}$ and $K_r^{(ij)(3)}$ are the modal stiffness, mass, and nonlinear modal stiffness coefficients of the rth mode of the (ij)th resonator, $\delta(\mathbf{x} - \mathbf{x}^{(ij)})$ is the 2D Dirac-delta function introduced to represent the inertia force of the (ij)th resonator at its reference position. Note that the linear and nonlinear modal properties of the resonators do not vary across the 2D lattice since the resonators are periodically repeated. This allows us to drop the superscript (ij) for ease of notation.

3 Nonlinear plane-wave expansion method

According to the Floquet–Bloch Theorem, the solution is assumed to be periodic with fundamental wavelength a given by the unit cell inter-distance (i.e., fundamental wave numbers $G_1 = G_2 = 2\pi/a$) and amplitude modulated by wave numbers k_1 and k_2 (i.e., wave lengths $\beta_1 = 2\pi/k_1$ and $\beta_2 = 2\pi/k_2$). Therefore, $w(x_1, x_2, t) = W(x_1, x_2, t)e^{-i(k_1x_1 + k_2x_2)}$ where $W(x_1, x_2, t)$ are periodic solutions of wavelength a, namely, $W(x_1 + a, x_2, t) = W(x_1, x_2, t)$, $W(x_1, x_2 + a, t) = W(x_1, x_2, t)$. Assuming a quasi-periodic solution of Eq. (4) according to the Floquet–Bloch theory from the outset to obtain the wave propagation equations for a subsequent asymptotic treatment is equivalent to solving the equations of motion (4) according to a perturbation scheme whereby the Floquet–Bloch solution is assumed at each order of the perturbation hierarchy [36].

A Fourier series representation of $W(x_1, x_2, t)$ is assumed as

$$W(x_1, x_2, t) = \sum_m \sum_n W_{mn}(t) e^{-iG_1^{(m)}x_1} e^{-iG_2^{(n)}x_2}, \tag{5}$$

where $G_1^{(m)} = mG_1$ and $G_2^{(n)} = nG_2$ are integer multiples of the fundamental wave numbers G_1 and G_2. This leads to cast the solution in the form

$$\begin{aligned}
w(x_1, x_2, t) \; &= \sum_m \sum_n W_{mn}(t) e^{-i(G_1^{(m)} + k_1)x_1} \\
&\quad e^{-i(G_2^{(n)} + k_2)x_2}.
\end{aligned} \tag{6}$$

Note that, upon considering $\boldsymbol{x}^{(ij)} = (i\boldsymbol{a}_1 + j\boldsymbol{a}_2)$ such that $e^{-iG_1^{(m)}x_1^{(ij)}} = 1$, $e^{-iG_2^{(n)}x_2^{(ij)}} = 1$, where $i, j = -\infty, \ldots, \infty$, one obtains the following key result:

$$\begin{aligned}
&w(x_1^{(ij)}, x_2^{(ij)}, t) \\
&= \sum_m \sum_n W_{mn}(t) e^{-i(G_1^{(m)} + k_1)x_1^{(ij)}} e^{-i(G_2^{(n)} + k_2)x_2^{(ij)}} \\
&= \sum_m \sum_n W_{mn}(t) e^{-iG_1^{(m)}x_1^{(ij)}} e^{-iG_2^{(n)}x_2^{(ij)}} \\
&e^{-i(k_1x_1^{(ij)} + k_2x_2^{(ij)})} \\
&= w_0(t) e^{-i(k_1x_1^{(ij)} + k_2x_2^{(ij)})}
\end{aligned} \tag{7}$$

where

$$w_0(t) := w(0,0,t) = \sum_m \sum_n W_{mn}(t). \tag{8}$$

Similarly, for the rth resonator at position $(x_1^{(ij)}, x_2^{(ij)})$,

$$z_r^{(ij)}(t) = z_{0r}(t) e^{-i(k_1 x_1^{(ij)} + k_2 x_2^{(ij)})}, \tag{9}$$

where

$$z_{0r}(t) := z_r^{(ij)}(0,0,t) = \sum_m \sum_n Z_{mn}^{(r)}(t). \tag{10}$$

It follows that the accelerations are expressed as

$$\begin{aligned} &\ddot{w}(x_1^{(ij)}, x_2^{(ij)}, t) = \ddot{w}_0(t) e^{-i(k_1 x_1^{(ij)} + k_2 x_2^{(ij)})}, \\ &\ddot{z}_r^{(ij)}(x_1^{(ij)}, x_2^{(ij)}, t) = \ddot{z}_{0r}(t) e^{-i(k_1 x_1^{(ij)} + k_2 x_2^{(ij)})}. \end{aligned} \tag{11}$$

Thus, the distribution of inertia forces induced by the resonators on the hosting structure can be expressed as

$$\begin{aligned} &\sum_{i,j} M_r^{(ij)} \left[\ddot{w}_0(t) + \ddot{z}_{0r}(t)\right] e^{-i(k_1 x_1^{(ij)} + k_2 x_2^{(ij)})} \\ &\quad \delta(\mathbf{x} - \mathbf{x}^{(ij)}) \\ &\quad = M_r \left[\ddot{w}_0(t) + \ddot{z}_{0r}(t)\right] e^{-i(k_1 x_1 + k_2 x_2)} \\ &\quad \sum_{i,j} \delta(\mathbf{x} - \mathbf{x}^{(ij)}) \end{aligned} \tag{12}$$

given that $M_r = M_r^{(ij)}$ and $e^{-i(k_1 x_1^{(ij)} + k_2 x_2^{(ij)})} \delta(\mathbf{x} - \mathbf{x}^{(ij)}) = e^{-i(k_1 x_1 + k_2 x_2)} \delta(\mathbf{x} - \mathbf{x}^{(ij)})$. The function $g(\mathbf{x}) := \sum_{i,j} \delta(\mathbf{x} - \mathbf{x}^{(ij)})$ is a periodic distribution of delta-Dirac functions, hence it can be expressed in Fourier series as

$$\begin{aligned} g(\mathbf{x}) =& \sum_{i=-\infty}^{\infty} \sum_{j=-\infty}^{\infty} \delta(\mathbf{x} - \mathbf{x}^{(ij)}) \\ =& \sum_m \sum_n g_{mn} e^{-i(G_1^{(m)} x_1 + G_2^{(n)} x_2)} \\ =& \frac{1}{a^2} \sum_m \sum_n e^{-i(G_1^{(m)} x_1 + G_2^{(n)} x_2)}, \\ g_{mn} :=& \frac{1}{a^2} \int_{-a/2}^{a/2} \int_{-a/2}^{a/2} \delta(\mathbf{x} - \mathbf{x}^{(ij)}) \\ & \times e^{-i(G_1^{(m)} x_1 + G_2^{(n)} x_2)} dx_1 dx_2 \\ =& \frac{1}{a^2} \end{aligned} \tag{13}$$

Therefore, the distribution of inertia forces reads:

$$M_r \left[\ddot{w}_0(t) + \ddot{z}_{0r}(t)\right] \frac{1}{a^2} e^{-i(k_1 x_1 + k_2 x_2)} \sum_{m,n} e^{-i(G_1^{(m)} x_1 + G_2^{(n)} x_2)}. \tag{14}$$

Let $M_r^* = M_r / a^2$, thus the equation of motion can be expressed as

$$\begin{aligned} &\rho^\star h \sum_m \sum_n \ddot{W}_{mn}(t) e^{-i(G_1^{(m)} x_1 + G_2^{(n)} x_2)} e^{-i(k_1 x_1 + k_2 x_2)} \\ &\quad + \sum_m \sum_n \kappa W_{mn}(t) e^{-i(G_1^{(m)} x_1 + G_2^{(n)} x_2)} e^{-i(k_1 x_1 + k_2 x_2)} \\ &\quad + \sum_r M_r^* \left[\ddot{w}_0(t) + \ddot{z}_{0r}(t)\right] \\ &\quad \sum_m \sum_n e^{-i(G_1^{(m)} x_1 + G_2^{(n)} x_2)} e^{-i(k_1 x_1 + k_2 x_2)} = 0, \end{aligned} \tag{15}$$

where $\kappa = D_{11}^*(G_1^{(m)} + k_1)^4 + 2(D_{12}^* + 2D_{66}^*)(G_1^{(m)} + k_1)^2 (G_2^{(n)} + k_2)^2 + D_{22}^* (G_2^{(n)} + k_2)^4$. Moreover,

$$\begin{aligned} &e^{-i(k_1 x_1 + k_2 x_2)} \sum_m \sum_n \Big\{ \rho^\star h \ddot{W}_{mn}(t) + \kappa W_{mn}(t) \\ &\quad + \sum_r M_r^* \left[\ddot{w}_0(t) + \ddot{z}_{0r}(t)\right] \Big\} \\ &\quad e^{-i(G_1^{(m)} x_1 + G_2^{(n)} x_2)} = 0. \end{aligned} \tag{16}$$

To satisfy the equation of motion at any (x_1, x_2), we apply the harmonic balance method by ensuring that each harmonic term vanishes. That is,

$$\begin{aligned} &\rho^\star h \ddot{W}_{mn}(t) + \kappa W_{mn}(t) \\ &\quad + \sum_{r=1}^{R} \left[M_r^* \left(\sum_{m=-N}^{N} \sum_{n=-N}^{N} \ddot{W}_{mn}(t) + \ddot{z}_{0r}(t) \right) \right] = 0, \\ &\quad m, n = -N, \ldots, N, \ r = 1, \ldots, R, \end{aligned} \tag{17}$$

where N is the number of retained harmonics, $z_{0r}(t) = \sum_m \sum_n Z_{mn}^{(r)}(t)$ as defined before. At the same time, the equations for the rth mode of the periodically distributed resonators read

$$\begin{aligned} &M_r^* \left(\sum_{m=-N}^{N} \sum_{n=-N}^{N} \ddot{W}_{mn}(t) + \ddot{z}_{0r}(t) \right) \\ &\quad e^{-i(k_1 x_1^{(ij)} + k_2 x_2^{(ij)})} + K_r z_{0r}(t) e^{-i(k_1 x_1^{(ij)} + k_2 x_2^{(ij)})} \\ &\quad + K_r^{(3)} (z_{0r}(t))^3 e^{-3i(k_1 x_1^{(ij)} + k_2 x_2^{(ij)})} = 0. \end{aligned} \tag{18}$$

Equation (18) upon multiplication by $e^{i(k_1 x_1^{(ij)} + k_2 x_2^{(ij)})}$ yields

$$\begin{aligned} &M_r^* \left(\sum_{m=-N}^{N} \sum_{n=-N}^{N} \ddot{W}_{mn}(t) + \ddot{z}_{0r}(t) \right) \\ &\quad + K_r z_{0r}(t) + K_{r*}^{(3)} (z_{0r}(t))^3 = 0, \end{aligned} \tag{19}$$

where $K_{r*}^{(3)} = K_r^{(3)} e^{-2i(k_1 x_1^{(ij)} + k_2 x_2^{(ij)})}$. The equation governing wave propagation depends only on the motion of the resonator at $\mathbf{x}_0 = 0$. This leads us to consider $K_{r*}^{(3)} = K_r^{(3)} e^{-2i(k_1 0 + k_2 0)} = K_r^{(3)}$. Therefore, the final equations for wave propagation across the metamaterial are

$$\begin{aligned}
&\rho^\star h \ddot{W}_{mn}(t) + \kappa W_{mn}(t) \\
&\quad + \sum_{r=1}^{R} \left[M_r^* \left(\sum_{m=-N}^{N} \sum_{n=-N}^{N} \ddot{W}_{mn}(t) + \ddot{z}_0^{(r)}(t) \right) \right] = 0, \\
&\quad m, n = -N, \ldots, N \\
&M_r^* \left(\sum_{m=-N}^{N} \sum_{n=-N}^{N} \ddot{W}_{mn}(t) + \ddot{z}_{0r}(t) \right) \\
&\quad + K_r z_{0r}(t) + K_r^{(3)} (z_{0r}(t))^3 = 0, \quad r = 1, \ldots, R.
\end{aligned} \tag{20}$$

Upon introducing the following nondimensional variables and parameters:

$$\begin{aligned}
&\tilde{x}_1 = \frac{x_1}{a}, \ \tilde{x}_2 = \frac{x_2}{a}, \ \tilde{t} = \omega_0 t, \ \ \omega_0 = \sqrt{\frac{D_{11}^*}{\rho^* h a^4}}, \\
&\tilde{W}_{mn} = \frac{W_{mn}}{a}, \ \ \tilde{z}_{0r} = \frac{z_{0r}}{a}, \\
&\tilde{\mathbf{x}}^{(ij)} = \frac{\mathbf{x}^{(ij)}}{a}, \ \ \tilde{\mathbf{k}} = \mathbf{k} a, \ \ \tilde{D}_{12} = \frac{D_{12}^*}{D_{11}^*}, \\
&\tilde{D}_{22}^* = \frac{D_{22}^*}{D_{11}^*}, \quad \tilde{D}_{66} = \frac{D_{66}^*}{D_{11}^*}, \\
&\tilde{M}_r = \frac{M_r}{\rho^* h a^2}, \ \ \tilde{K}_r = \frac{K_r a^2}{D_{11}^*}, \ \ \tilde{K}_r^{(3)} = \frac{K_r^{(3)} a^4}{D_{11}^*}.
\end{aligned} \tag{21}$$

The nondimensional equations of motion of the coupled system read:

$$\begin{aligned}
&\ddot{\tilde{W}}_{mn}(t) + \tilde{\kappa} \tilde{W}_{mn}(t) \\
&\quad + \sum_{r=1}^{R} \left[\tilde{M}_r \left(\sum_{m=-N}^{N} \sum_{n=-N}^{N} \ddot{\tilde{W}}_{mn}(t) \right. \right. \\
&\quad \left. \left. + \ddot{\tilde{z}}_{0r}(t) \right) \right] = 0, \quad m, n = -N, \ldots, N, \\
&\tilde{M}_r \left(\sum_{m=-N}^{N} \sum_{n=-N}^{N} \ddot{\tilde{W}}_{mn}(t) + \ddot{\tilde{z}}_{0r}(t) \right) \\
&\quad + \tilde{K}_r \tilde{z}_{0r}(t) + \tilde{K}_r^{(3)} (\tilde{z}_{0r}(t))^3 = 0, \quad r = 1, \ldots, R,
\end{aligned} \tag{22}$$

where $\tilde{\kappa} = (G_1^{(m)} + \tilde{k}_1)^4 + 2(\tilde{D}_{12}^* + 2\tilde{D}_{66}^*)(G_1^{(m)} + \tilde{k}_1)^2 (G_2^{(n)} + \tilde{k}_2)^2 + \tilde{D}_{22}^* (G_2^{(n)} + \tilde{k}_2)^4$. Equation (22) can be recast as:

$$\mathbf{M}\ddot{\mathbf{u}} + \mathbf{K}\mathbf{u} = \mathbf{0}, \tag{23}$$

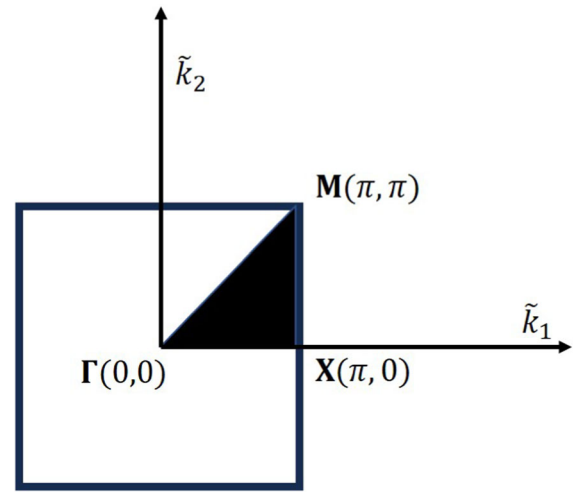

Fig. 2 The first irreducible Brillouin zone

with $\mathbf{u} = [\tilde{W}_{-N-N}, \ldots, \tilde{W}_{00}, \ldots, \tilde{W}_{NN}, \tilde{z}_{01}, \ldots, \tilde{z}_{0R}]^\top$.

The nondimensional wave numbers $\tilde{k}_1$ and $\tilde{k}_2$ within the irreducible Brillouin zone (IBZ) exhibit the following ranges (see Fig. 2): $\mathbf{\Gamma X}$, $\boldsymbol{XM}$, $\boldsymbol{M\Gamma}$. The wave numbers $(\tilde{k}_1, \tilde{k}_2)$ should be within the triangular range formed by the three vertices ($\mathbf{\Gamma}$, $\boldsymbol{X}$, $\boldsymbol{M}$).

4 Dispersion functions

4.1 Linear dispersion functions and eigenvectors

First the linear dispersion properties are tackled as a basis to solve the nonlinear problem. To this end, by dropping the nonlinear terms in Eqs. (20) and letting $\tilde{W}_{mn}(t) = \tilde{W}_{mn} e^{i\omega t}$ and $\tilde{z}_{0r}(t) = \tilde{Z}_r e^{i\omega t}$, the resulting equations of motion become the following eigenvalue problem:

$$\begin{aligned}
&-\omega^2 \tilde{W}_{mn} + \tilde{\kappa} \tilde{W}_{mn} - \omega^2 \\
&\quad \sum_r \tilde{M}_r \left(\sum_{m=-N}^{N} \sum_{n=-N}^{N} \tilde{W}_{mn} + \tilde{Z}_r \right) = 0, \\
&\quad m, n = -N, \ldots N \\
&-\omega^2 \tilde{M}_r \left(\sum_{m=-N}^{N} \sum_{n=-N}^{N} \tilde{W}_{mn} + \tilde{Z}_r \right) \\
&\quad + \tilde{K}_r \tilde{Z}_r = 0, \quad r = 1, \ldots, R
\end{aligned} \tag{24}$$

which can be rewritten as $(\mathbf{K} - \omega^2 \mathbf{M})\mathbf{u} = \mathbf{0}$. The linear dispersion equation is given by $\det(\mathbf{K} - \omega^2 \mathbf{M}) = 0$,

whose roots, denoted by ω_n, describe the frequencies of the propagation modes $\boldsymbol{\phi}_n$ obtained, in turn, as eigensolutions. The application of the cell projection method entails retaining the fundamental harmonic only in the harmonic series of the PWE method. The resulting equations in this instance allow to obtain the closed-form expressions for the linear frequencies of the fundamental propagation mode, facilitating the determination of the lowest stopband properties [34,36]. On the other hand, upon utilizing the PWE method with an arbitrary number of series terms, Eq. (24) proves too complex to yield closed-form solutions for the frequencies.

4.2 Nonlinear dispersion properties

By employing the mass-normalized modal matrix $\Phi = [\boldsymbol{\phi_1}, \boldsymbol{\phi_2}, \ldots, \boldsymbol{\phi_{S+R}}]$, which collects S+R eigenvectors, where $S = (2N+1)^2$ is the total number of harmonics retained in the system, and by introducing the change of coordinates $\mathbf{u} = \boldsymbol{\Phi q}$, with $\mathbf{q} = [q_1, q_2, \ldots, q_{S+R}]^\top$ being the principal coordinates vector, Eq. (22) can be rewritten as the following matrix-valued equation:

$$\mathbf{M\Phi\ddot{q}} + \boldsymbol{K\Phi q} = \boldsymbol{K^{(3)}(\Phi q, \Phi q, \Phi q)}, \tag{25}$$

whose $\boldsymbol{K^{(3)}(\Phi q, \Phi q, \Phi q)}$ is the vector of the nonlinear forces (whose expression is given in Eq. (27)). Equation (25), upon pre-multiplication by $\boldsymbol{\Phi}^\top$, yields the linearly decoupled system of modal equations:

$$\ddot{\mathbf{q}} + \boldsymbol{\Lambda q} = \boldsymbol{c(q, q, q)}, \tag{26}$$

where $\boldsymbol{\Lambda} = \mathrm{diag}(\omega_1^2, \omega_2^2, \ldots, \omega_{S+R}^2)$ and

$$\begin{aligned}\mathbf{c}(\boldsymbol{q, q, q}) &= \boldsymbol{\Phi}^\top \boldsymbol{K^{(3)}(\Phi q, \Phi q, \Phi q)} \\ &= \boldsymbol{\Phi}^\top \begin{bmatrix} \mathbf{0} \\ \ldots \\ \mathbf{0} \\ -\tilde{K}_1^{(3)}(\boldsymbol{\phi}_{(S+1)}^\top \boldsymbol{q})(\boldsymbol{\phi}_{(S+1)}^\top \boldsymbol{q})(\boldsymbol{\phi}_{(S+1)}^\top \boldsymbol{q}) \\ \ldots \\ -\tilde{K}_R^{(3)}(\boldsymbol{\phi}_{(S+R)}^\top \boldsymbol{q})(\boldsymbol{\phi}_{(S+R)}^\top \boldsymbol{q})(\boldsymbol{\phi}_{(S+R)}^\top \boldsymbol{q}) \end{bmatrix},\end{aligned} \tag{27}$$

where $\boldsymbol{\phi_{(n)}} = \boldsymbol{\Phi}^\top \cdot \mathbf{e}_n$ are the column vectors collecting the nth rows of the mass-normalized modal matrix $\boldsymbol{\Phi}$, respectively, $\mathbf{e}_n = [\delta_{1n}, \delta_{2n}, \ldots, \delta_{(S+R)n}]^\top$.

The asymptotic method of multiple scales can be effectively employed to analyse the nonlinear wave properties of the considered metamaterial with the embedded membrane resonators. To this end, the solution is expressed as a series of the small nondimensional book-keeping parameter ε, where each term in the series is a function of two time scales $T_j = \varepsilon^j t$ for $j = 0, 2$, according to

$$\mathbf{q}(t;\varepsilon) = \varepsilon \mathbf{q}_1(T_0, T_2) + \varepsilon^3 \mathbf{q}_3(T_0, T_2) + O(\varepsilon^5). \tag{28}$$

By considering the change of time variables, the derivatives with respect to the actual time are expressed as: $\partial(\cdot)/\partial t = D_0 + \varepsilon^2 D_2$, and $\partial^2(\cdot)/\partial t^2 = D_0^2 + 2\varepsilon^2 D_0 D_2$, where $D_j(\cdot) := \partial(\cdot)/\partial T_j$. By equating all terms of like powers of ε to zero, the following hierarchy of problems is obtained:

$$\text{Order}(\varepsilon):$$

$$D_0^2 \mathbf{q}_1 + \boldsymbol{\Lambda q}_1 = \mathbf{0}, \tag{29a}$$

$$\text{Order}(\varepsilon^3):$$

$$D_0^2 \mathbf{q}_3 + \boldsymbol{\Lambda q}_3 = -2D_0 D_2 \mathbf{q}_1 + \mathbf{c}(\mathbf{q}_1, \mathbf{q}_1, \mathbf{q}_1). \tag{29b}$$

Here we focus on the special case of unit cells with R nonlinear modal resonators. Accordingly, the generating solution of the first order problem given by Eq. (29a) can be expressed in the form:

$$\begin{aligned}\mathbf{q_1} &= \begin{bmatrix} q_{1,1} \\ \ldots \\ q_{1,S+R} \end{bmatrix} \\ &= \begin{bmatrix} A_1(T_2)\exp(i\omega_1 T_0) \\ \ldots \\ A_{S+R}(T_2)\exp(i\omega_{S+R} T_0) \end{bmatrix} + c.c.\end{aligned} \tag{30}$$

where $A_j(T_2)$ are complex-valued amplitudes and $c.c.$ stands for the complex conjugate of the preceding terms. The cubic perturbation problem expressed by Eq. (29b) contains resonant terms due to the cubic nonlinearity which can cause secular terms if not removed. By enforcing the solvability condition in the nth propagation mode, and assuming that the frequencies ω_n are away from the condition $\omega_n \approx 3\omega_m$ so as to prevent the onset of 3:1 internal resonances, one finally obtains the modulation equation:

$$2i\omega_n D_2 A_n = \boldsymbol{\phi}_n^{\top} \begin{bmatrix} 0 \\ \dots \\ 0 \\ -\tilde{K}_1^{(3)}(3\phi_{S+1,n}^3 A_n^2 \bar{A}_n + 6\phi_{S+1,n} A_n \sum_{i=1}^{S+R}[\phi_{S+1,i}^2 A_i \bar{A}_i (1-\delta_{in})]) \\ \dots \\ -\tilde{K}_R^{(3)}(3\phi_{S+R,n}^3 A_n^2 \bar{A}_n + 6\phi_{S+R,n} A_n \sum_{i=1}^{S+R}[\phi_{S+R,i}^2 A_i \bar{A}_i (1-\delta_{in})]) \end{bmatrix} \tag{31}$$

where $\phi_{i,j}$ represents the modal component of the ith row and jth column of Φ.

To obtain the real-valued form of Eq. (31), one has to express A_n in its polar form as

$$A_n(T_2) = \tfrac{1}{2} a_n(T_2) \exp(i\theta_n(T_2)), \tag{32}$$

where a_n and θ_n are the unknown amplitude and phase of the nth propagation mode, respectively. By substituting Eq. (32) into Eq. (31) and separating real and imaginary parts in Eq. (31), one obtains:

$$\begin{aligned} a_n^{'} &= 0, \\ \theta_n^{'} &= \frac{3\sum_r \tilde{K}_r^{(3)}(\phi_{S+r,n}^4 a_n^2 + 2\phi_{S+r,n}^2 \sum_{s=1}^{S+R}[\phi_{S+r,s}^2 (1-\delta_{sn}) a_s^2])}{8\omega_n}, \end{aligned} \tag{33}$$

where the prime indicates differentiation with respect to the slow time scale T_2. Finally, by re-absorbing ε in the amplitude definition, the nonlinear frequencies of the propagation modes are expressed as

$$\omega_{nl}^{(n)} = \omega_n + \frac{3\sum_r \tilde{K}_r^{(3)}(\phi_{S+r,n}^4 a_n^2 + 2\phi_{S+r,n}^2 \sum_{s=1}^{S+R}[\phi_{S+r,s}^2 (1-\delta_{sn}) a_s^2])}{8\omega_n}, \tag{34}$$

with $n = 1, 2, \dots, (S+R)$.

5 Numerical simulations

Numerical computations are carried out to investigate first the linear dispersion properties and, subsequently, the effects of the resonator nonlinearity. The objective is to provide an optimization strategy of the resonators design embedded in a given metamaterial. Square lattices are considered with the following parameters for the numerical simulations: characteristic length $a = 0.14$ m, plate thickness $h = 0.005$ m, wall width $t_h = 0.0025$ m, mass density of the hosting structure $\rho = 1,150$ kg/m^3, Young's modulus $E = 2.2$ GPa, shear modulus $G = 0.85$ GPa, Poisson's ratio $\nu = 0.35$. The equivalent mass of a single square cell of the hosting structure is computed as $\rho^* h a^2$. The parameters for the membrane resonators are: side length $l_m = a - 2t_h$, membrane thickness $h_m = 0.1$ mm, mass density of the membrane material $\rho_m = 1,150$ kg/m^3, Young's modulus $E_m = 2.2$ GPa. The pre-stress of the resonating membranes caused by the tension $n^{(0)}$ due to the piezoelectric effect is set to be $12N/m$, and the ratio μ between the center mass $M^{(C)}$ and the mass of the bare membrane is set to be 6, such that, for the conducted numerical tests, stopbands are manifested in a relatively low frequency range. The relationship between the nondimensional modal parameters ($\tilde{M}_{mn}$, $\tilde{K}_{mn}$) and the physical parameters (μ, $n^{(0)}$) is expressed as:

$$\begin{aligned} \tilde{K}_{mn} &= \tilde{n}^{(0)}(\tfrac{\pi}{2})^2(m^2+n^2), \quad \tilde{n}^{(0)} = n^{(0)} a^2 / D_{11}^* \\ \tilde{M}_{mn} &= [\mu \sin^2(\tfrac{m\pi}{2}) \sin^2(\tfrac{n\pi}{2}) \\ &\quad + \tfrac{1}{4}](\rho_m h_m l_m^2)/(\rho^* h a^2). \end{aligned} \tag{35}$$

5.1 Linear dispersion properties

The absence of a closed-form expression when applying the full PWE method poses a significant challenge in conducting optimization studies similar to those previously accomplished [34]. However, employing numerical comparisons facilitates a comprehensive understanding of the relationship and comparative performance of the two methods, thereby enhancing the approach to optimization.

5.1.1 Comparing the cell projection method solution with the PWE

In this section, a comparison of the results obtained by the PWE method and the cell projection method is carried out when only one stopband is formed due to the truncation of the cellular membrane modes to one vibration mode. In this context, when applying the projection method, the wave dispersion properties are characterized by the presence of a low-frequency acoustic mode and a high-frequency optical mode. On the other hand, with the full PWE method, all propagating modes are taken into account, achieving a more comprehensive overview of the dispersion properties. However, despite its comprehensiveness, the PWE method lacks closed-form expressions for the band gap properties.

Figure 3a depicts the dispersion curves of the bare plate (i.e., without resonators, hence, without stopbands), obtained by applying the PWE method (blue) with $N = 3$ and the Projection method (black dashed lines). This figure proves a perfect agreement between the results obtained with the two methods. It should be noted that the dispersion curves are overlapped in the interested low frequency range when $N \geq 3$. For simplicity, in Sect. 5, $N = 3$ will be applied unless otherwise specified.

On the other hand, Fig. 3b presents the linear dispersion curves for the case in which the resonators induce the emergence of a fundamental stopband (here, $\mu = 6$ and $\tilde{n}^{(0)} = 0.5747$). A comparison between the projection method solution (black dashed) and the PWE method solution with retained harmonics $N = 0$ (red) and $N = 3$ (blue) reveals that the dispersion properties obtained by the projection method and the PWE method with $N = 0$ are very similar, while the PWE method with $N = 3$ is able to capture all the propagating modes. Therefore, the projection method coalesces into a particular or simplified case of the PWE method when only one harmonic is retained. A zoomed-in view of the band gap is provided in Fig. 3b, where it can be observed that the solution obtained with the projection method is not exactly the same as that obtained with the PWE method with $N = 0$, but it gets much closer to the PWE method solution with $N = 3$. Overall, the difference between the solutions obtained with the two methods is around 0.5% and thus can be considered negligible.

5.1.2 Parametric studies within the linear framework

As shown in the authors' previous study [34], the stopband was obtained within the range of the first propagating mode between the minimum linear optical frequency and the maximum linear acoustic frequency by employing the cell projection method. Moreover, the sensitivity of the stopband with respect to the resonator parameters μ and $\tilde{n}_0$ was investigated. This knowledge can be utilized to fine-tune the membrane parameters to meet specific requirements, allowing for semi-adaptive control over wave propagation. This approach is particularly valuable, as the fundamental stopband is crucial in the vast majority of applications.

Upon applying the PWE method as done in the present work, the lack of closed form expressions of the stopband makes the study more challenging. We first consider four cases with only one resonator whose parameters are set to $\mu = 1$ while the prestress attains one of the following values: $\tilde{n}_0 = (0.2395, 0.4790, 0.9580, 1.1975)$. This allows us to study how the stopband position is affected by the local resonance frequency. Figure 4a, b reveal that there is a complete stopband for all wavenumbers and an incomplete stopband in the wavenumber range $\Gamma - X$, with an increasing frequency of the band gap, and with the absolute stopband widths becoming wider. In Fig. 4c, there seems to occur a topological change of the optical mode and the complete stopband becomes relatively narrow. In addition, there is an incomplete stopband (cyan) in the range $M - \Gamma$. In Fig. 4d, the complete stopband disappears and only two incomplete stopbands exist.

5.2 Nonlinear dispersion properties

In the nonlinear wave propagation regime the modal amplitudes notably affect the dispersion properties. With the PWE-based solution, the complexity of the system of $(2N + 1)^2 + R$ equation, makes it hard to comprehensively analyze the nonlinear effect of each individual modal amplitude. In addition, with the projection method, the modal amplitudes respectively denoted by a^- and a^+ have the meaning of amplitudes of the acoustic and optical modes, respectively.

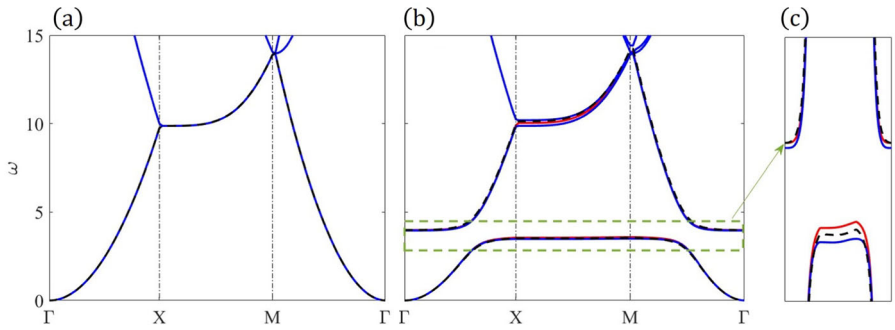

Fig. 3 The dispersion curves of the metamaterial obtained with the PWE method (blue for $N = 3$ and red for $N = 0$) and the projection method (black dashed): Part (**a**) shows the case of the bare plate without resonators; part (**b**) shows the case exhibiting one stopband with the resonators parameters set to $\mu = 6$ and $\tilde{n}^{(0)} = 0.5747$. (Color figure online)

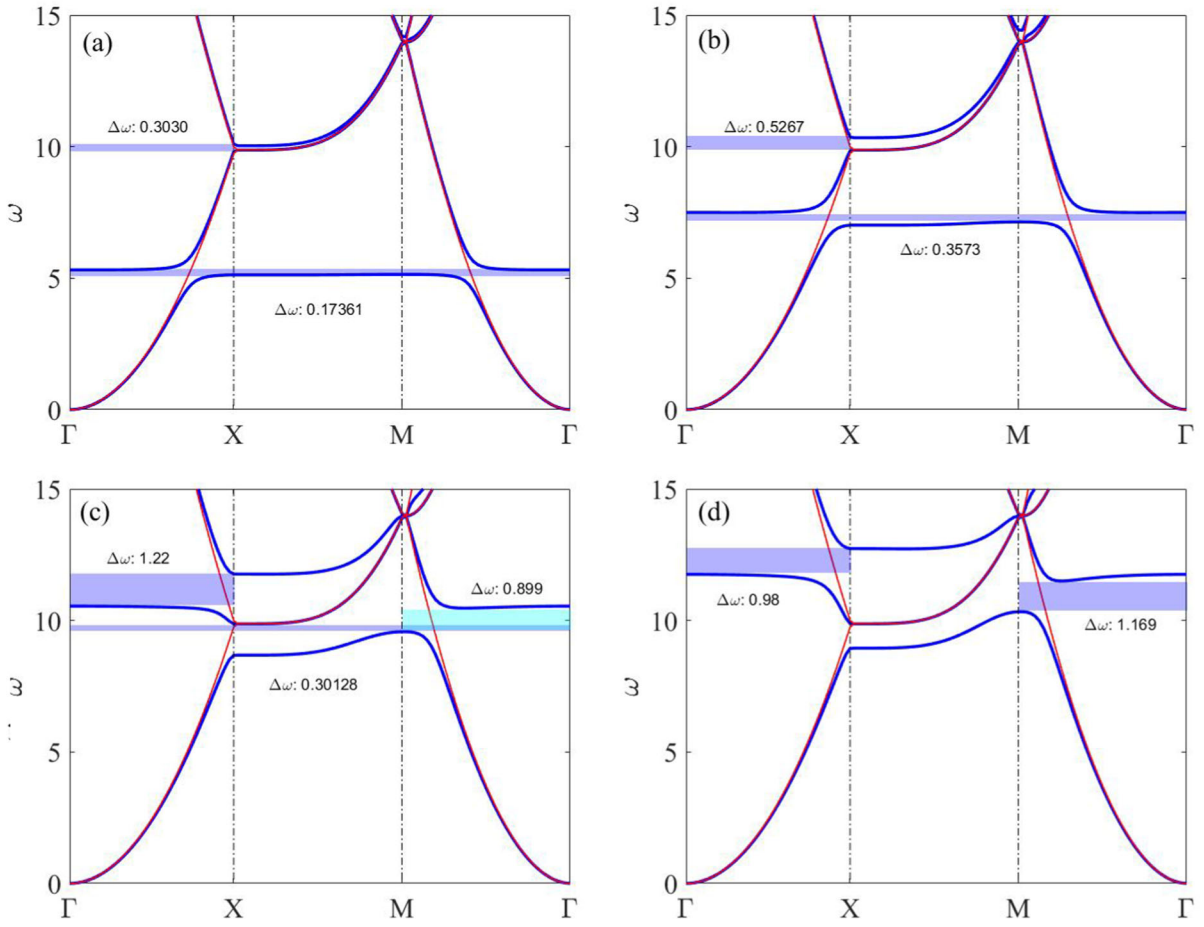

Fig. 4 The dispersion properties of the metamaterial with the resonators parameters set to $\mu = 1$ and $\tilde{n}_0 = (0.2395, 0.4790, 0.9580, 1.1975)$. The blue lines indicate the linear dispersion curves obtained by the PWE method. The filled blue or cyan regions represent the linear band gaps. The red lines represent the dispersion function of the bare plate. (Color figure online)

Since the two methods produce different equations of motion, the modal amplitudes have distinct interpretations. Therefore, a fair comparison between the two methods in the nonlinear regime is not straightforward.

To discuss the nonlinear effects on the stopband, the sensitivity of the stopband with respect to the resonators parameters is quantified by computing the ratio of the nth nonlinear stopband width to the nth corresponding linear stopband width, i.e.,

$$G_n = \frac{\max(\omega_{nl}^{(n+1)}) - \min(\omega_{nl}^{(n)})}{\max(\omega_{n+1}) - \min(\omega_n)}. \tag{36}$$

5.2.1 Examples of complete and incomplete stopbands

In this section, two examples are discussed to illustrate instances where the band gap extends beyond the first propagating mode, thus making the projection method inapplicable. In contrast, the implemented nonlinear version of the PWE method allows to predict linear and nonlinear dispersion properties for all propagation modes.

In the first example, the first symmetric mode of the membrane is considered with amplitude $a_n = 3\times10^{-3}$, giving rise to two incomplete stopbands beyond the first propagation mode. The linear (blue) and nonlinear (red) dispersion curves are shown in Fig. 5a. Similarly, the filled blue region represents the linear band gap while the red filled region indicates the nonlinear band gap. In the second example, the first two symmetric modes of the membrane are considered. They not only cause two complete stopbands but also an incomplete stopband beyond the first propagation mode.

Compared to the linear dispersion curves represented in blue, the nonlinear dispersion curves show hardening effects since all curves shift upward towards higher frequencies. Most importantly, for certain modal amplitudes, the bandwidth of all stopbands gets expanded ($G > 1$) because of the nonlinear resonance effects.

5.2.2 Numerical validation

The nonlinear dispersion properties are analytically computed using Eq. (34). However, the same curves are numerically obtained by time integrating the following system of equations obtained with the PWE method:

$$\begin{aligned}
&\ddot{\tilde{W}}_{mn}(t) + \tilde{c}_{mn}\dot{\tilde{W}}_{mn}(t) + \tilde{\kappa}\tilde{W}_{mn}(t) \\
&\quad + \sum_{r=1}^{R}\left[\tilde{M}_r\left(\sum_{m=-N}^{N}\sum_{n=-N}^{N}\ddot{\tilde{W}}_{mn}(t) + \ddot{\tilde{z}}_{0r}(t)\right)\right] \\
&= \tilde{F}_{mn},\ \tilde{M}_r\left(\sum_{m=-N}^{N}\sum_{n=-N}^{N}\ddot{\tilde{W}}_{mn}(t) + \ddot{\tilde{z}}_{0r}(t)\right) \\
&\quad + \tilde{K}_r\tilde{z}_{0r}(t) + \tilde{K}_r^{(3)}(\tilde{z}_{0r}(t))^3 = 0, r = 1, ..., R,
\end{aligned} \tag{37}$$

where linear damping is introduced for numerical reasons. The damping coefficient is set to $\tilde{c}_{mn} = 2\eta\sqrt{\tilde{\kappa}}$ with $\eta = 0.15$ to facilitate convergence towards the steady-state in a sufficiently short time overcoming excessively long transients, but it should be noted that, while light damping disrupts exact wave cancellation within the band gaps, optimal damping levels can minimize wave amplitudes across these regions as discussed in [37]. The excitation amplitudes are set to be $\tilde{F}_{mn} = 0.01$ for $m, n = -N, \ldots, N$ to make sure all propagation modes get excited. Further details about Eq. (37) are presented in "Appendix B". The resonators parameters are set to $\mu = 6$ and $\tilde{n}^{(0)} = 0.5747$. The explicit Runge–Kutta method (function "ode23" in Matlab) is used to integrate the equations yielding the time-dependent response. In these numerical computations, when the wave numbers or frequencies are relatively small, considerably large simulation times are necessary to reach steady-states. This implies a heavy computational burden. By taking into account the fact that such scenarios yield meaningless information, they are not tackled in the computations.

We collect the maximum displacement amplitudes of the plate, i.e., $\sum_{mn}\tilde{W}_{mn}$, at steady-state for every choice of wave number and excitation frequency. The results are shown in Fig. 6 in terms of contour plots where the horizontal axis denotes the wave number, the vertical axis indicates the non-dimensional harmonic excitation frequency, while the steady-state displacement amplitude levels are represented by colors, in particular, bright yellow means amplitudes beyond 1×10^{-3}, which is above 20% the plate thickness. Correspondingly for the damped wave propagation scenario here considered, the stopband is defined as the region where the wave amplitude is sufficiently small ($< 5\times10^{-4}$ for the first stopband and $< 2\times10^{-4}$ for the second stopband, respectively) across all wave numbers and excitation frequencies. Figure 6a shows

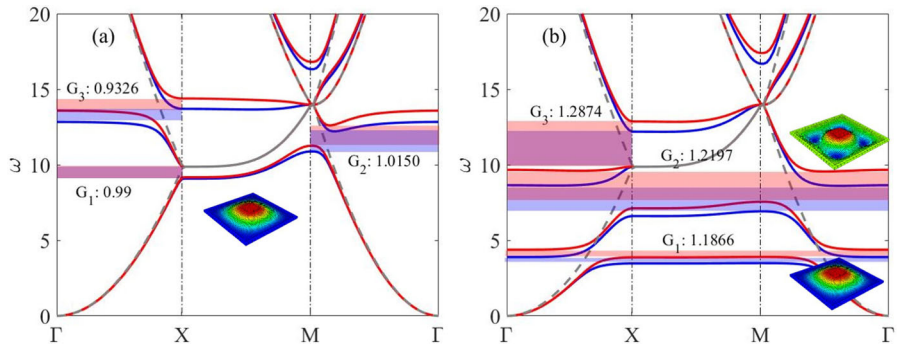

Fig. 5 The nonlinear dispersion curves of the metamaterial with the modal amplitude set to $a_n = 3 \times 10^{-3}$. The blue lines indicate the linear dispersion curves while the red curves indicate the nonlinear dispersion curves. The filled blue regions represent the linear band gap while the red regions indicate the nonlinear band gaps. The gray dashed lines represent the dispersion curves of the bare plate. The resonators parameters set to $\mu = 1$ and $\tilde{n}^{(0)} = 1.4367$ in part (**a**) while they set to $\mu = 6$ and $\tilde{n}^{(0)} = 0.5747$ in part (**b**). (Color figure online)

that the dispersion curves of the metamaterial with linear resonators, here described by red lines, fully match the numerically obtained time responses (alongside the middle of the yellow range). Moreover, the first stopband region goes from 3.5 to 3.8 while the second region spans the range from 7.5 to 8.5. On the other hand, Fig. 6b shows the case in which the resonators nonlinearity is turned on. The first stopband region gets enlarged from 4 to 4.4 and the second gets enlarged from 7.5 to 8.8, due to the hardening nonlinearity and damping effects. The corresponding 3D frequency-wave number response plots for the linear and nonlinear cases are shown in parts (c,d), respectively, to provide a more effective representation of the damped response amplitudes and the stopbands.

5.3 Semi-active wave propagation control

An advantageous aspect of the piezoelectric metamaterial design lies in the ability to tune the membrane parameters according to specific requirements to achieve semi-adaptive wave propagation control. The voltage applied to the piezoelectric membrane resonators effects changes in the membrane pre-stress and this results into a shift of the stopbands towards targeted frequency ranges.

Figure 7a shows the linear minimum frequency (red surface) and maximum frequency (blue) for the first stopband with respect to changes of the resonators mass ratio and membrane pretension, and the corresponding width of the first linear stopband is shown as a contour plot in 7b. The results highlight that, when the center mass becomes heavier, the linear stopband will decrease, and when the equivalent modal spring becomes stiffer, the stopband will have larger width and migrate towards higher frequencies. Moreover, one should note that with resonators lighter mass and stiffer springs (the left-upper corner in Fig. 7b), the stopband disappears in the region of the fundamental propagation mode as shown in Fig. 4d. The results facilitate the linear design process of the resonator parameters based on the stopband characteristic requirements.

In the authors' previous work [33,34,36], examples are provided to demonstrate how the analytical dispersion properties can facilitate the design of membrane resonators in the nonlinear range. Assuming the mass of the resonators has been set and the membrane pretension $\tilde{n}_0$ is the only tunable parameter, and the modal amplitudes for all modes are set to a certain range of values, one can apply the PWE method to obtain the dispersion curves and the band gaps width. The nonlinear effects depend quadratically on the modal amplitudes of all modes. Optimization of the parameters of the PVDF membrane resonators can be made by examining the resulting gain factor G.

Figure 8 shows the variation of the nonlinear stopband gain factor G for the metamaterial with membrane resonators whose mass is $\mu = 6$ and the modal amplitudes are set to: $a_n = 2 \times 10^{-4}$ (red) and $a_n = 2.5 \times 10^{-4}$ (blue) in terms of the pre-stress $\tilde{n}_0$. The corresponding linear and nonlinear band gap

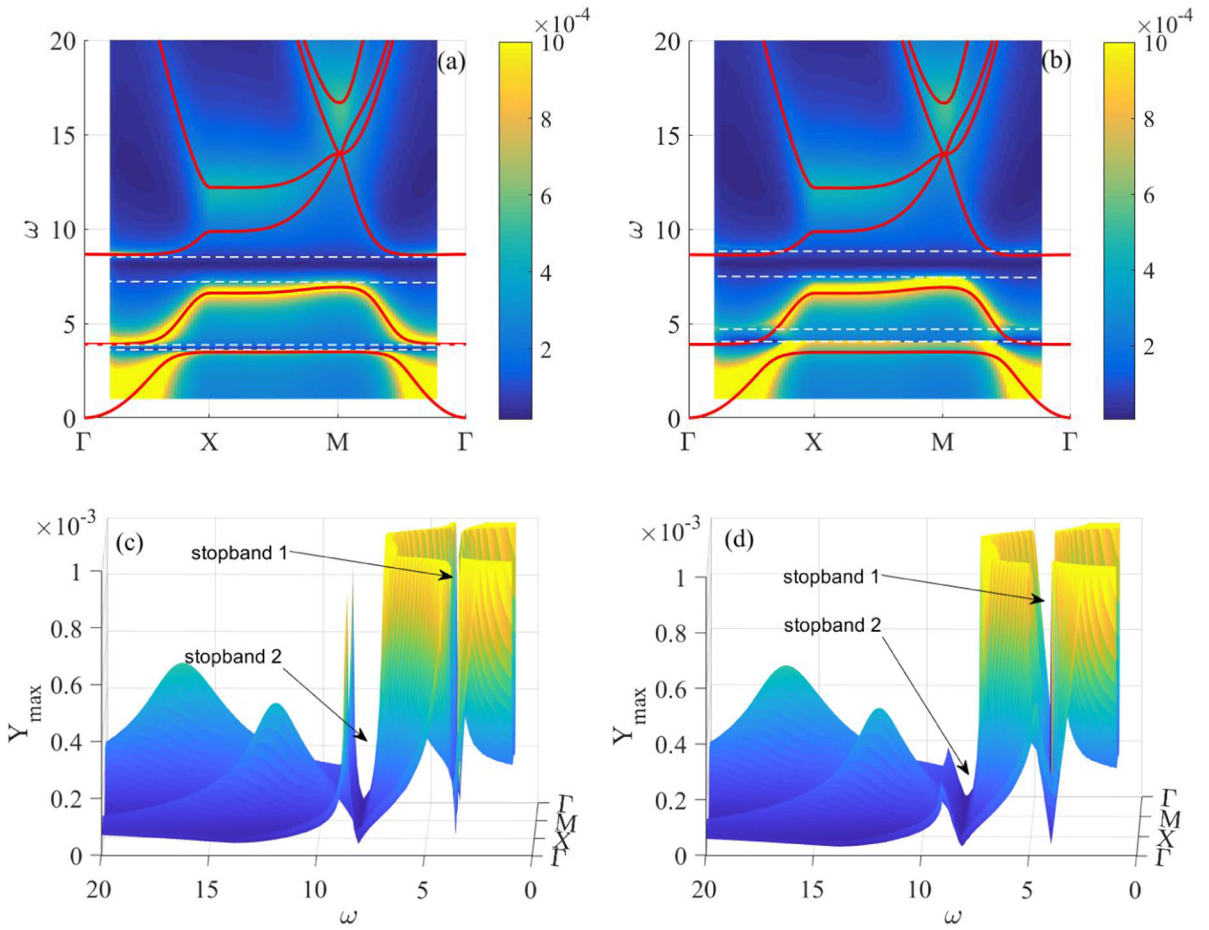

Fig. 6 **a**, **b** Contour plots showing the displacement amplitudes of the plate at steady-state for the metamaterial subject to harmonic excitation ($\tilde{F}_{mn} = 0.01$) and (**c**, **d**) the corresponding 3D plots. The red lines are the analytical linear dispersion curves. In parts (**a**, **c**) the resonators are linear, in parts (**b**, **d**) the resonators are nonlinear with hardening cubic nonlinearity. (Color figure online)

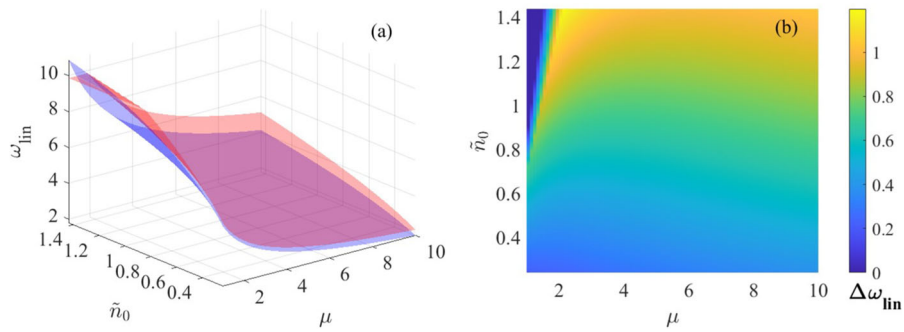

Fig. 7 **a** The linear minimum frequency of the optical mode (red surface) and maximum frequency of the acoustic mode (blue) for the first stopband with respect to changes of the resonators mass ratio and membrane pretension. **b** The width of the first linear stopband with respect to changes of the resonators mass ratio and membrane pretension. (Color figure online)

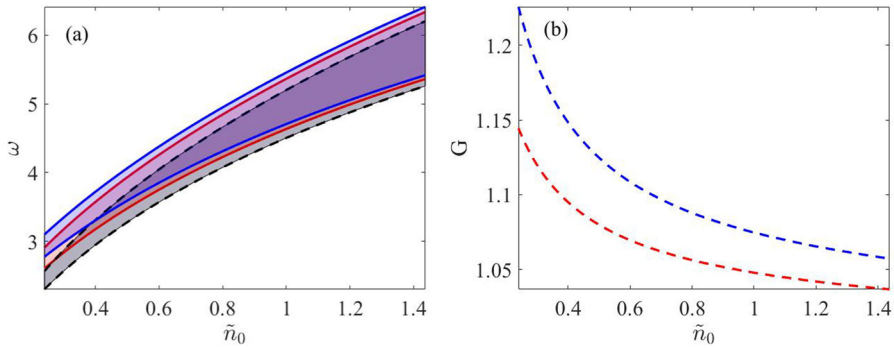

Fig. 8 **a** Variation of the linear (black region) and nonlinear band gap range for the metamaterial with membrane resonators having $\mu = 6$, modal amplitudes $a_n = 2 \times 10^{-4}$ (red region) and $a_n = 2.5 \times 10^{-4}$ (blue region). **b** The corresponding nonlinear stopband gain factor G with modal amplitudes set to: $a_n = 2 \times 10^{-4}$ (red) and $a_n = 2.5 \times 10^{-4}$ (blue) in terms of the pre-stress $\tilde{n}_0$. (Color figure online)

ranges are also presented. By choosing the resonator mass and letting the pre-stress $\tilde{n}_0$ be the only tunable parameter, such analysis is carried out for any combination of modal amplitudes, as it should be done in the design of the optimal parameters of the resonators.

6 Conclusions

In this paper, we investigated the nonlinear wave properties of square lattices incorporating membrane resonators. Using the Floquet–Bloch theorem and the plane-wave expansion (PWE) method, we derived the equations governing wave propagation. A significant contribution of this work is the extension of the PWE method to metamaterials with nonlinear resonators, which substantially broadens the applicability of this analytical approach to nonlinear systems. Building on our previous research [34], we provide a more comprehensive perspective by analytically computing nonlinear dispersive waves. This leads to a deeper understanding of the linear and nonlinear dispersion properties of the metamaterials. Through the utilization of multiple scales, we obtained the nonlinear dispersion functions. Numerical results revealed both the linear and nonlinear dispersion properties of the metamaterials, indicating the potential for designing metamaterials with multiple complete or incomplete band gaps with tunable frequencies by optimizing the resonator parameters. Our study underscores the potential of semi-adaptive tuning of resonator nonlinearity to enhance the controllability of wave propagation in metamaterials with appropriately designed nonlinear resonators.

Acknowledgements The authors thank Pranath Kumar Gourishetty for his technical assistance. This work was partially supported by the European Office of Aerospace Research and Development/Air Force Office of Scientific Research under Grant N. FA8655-20-1-7025 and by a MIUR (Italian Ministry of Education, Scientific Research and University) Grant 2017L7X3CS_002 and Project ECS 0000024 Rome Technopole, CUP B83C22002820006, National Recovery and Resilience Plan (NRRP) Mission 4 Component 2 Investment 1.5, funded by the European Union –NextGenerationEU.

Author contributions Yichang Shen wrote the first manuscript, and Walter Lacarbonara supervised this work. All authors developed the main concept together and reviewed the manuscript.

Funding The authors have not disclosed any funding.

Data availability No datasets were generated or analysed during the current study.

Declarations

Competing interests The authors declare no competing interests.

Appendix A The bending coefficients and the mass density of the equivalent orthotropic plate

The bending coefficients D_{11}^*, D_{12}^*, D_{22}^*, D_{66}^* and the density $\rho^\star$ of the equivalent orthotropic plate read:

$$D_{11}^* = D_{22}^* = \frac{Eh^3 t_h}{12a}, \quad D_{12}^* = 0,$$
$$D_{66}^* = \frac{h}{12}\left(\frac{Gt_h^3(1-\kappa)}{6}\right), \quad \rho^\star = \frac{t_h(2+a/h)}{a}\rho. \tag{A1}$$

where E is Young's modulus, G is the shear modulus of the lattice material, and

$$\kappa = \frac{96t_h}{\pi^5 h}\sum_{p=1}^{\infty}\Big[\frac{1-(-1)^p}{p^5}\tanh\left(\frac{p\pi h}{2t_h}\right)\Big]. \tag{A2}$$

Appendix B Equations of motion of the model with damping and external excitations

The equations of motion for the metamaterials considering damping c and external excitations F can be expressed as

$$\begin{aligned}
&\rho^\star h\frac{\partial^2 w(\mathbf{x},t)}{\partial t^2} + c\frac{\partial w(\mathbf{x},t)}{\partial t}\\
&+\left[D_{11}^*\frac{\partial^4 w(\mathbf{x},t)}{\partial x_1^4} + 2(D_{12}^*+2D_{66}^*)\frac{\partial^4 w(\mathbf{x},t)}{\partial x_1^2\partial x_2^2}\right.\\
&\left.+D_{22}^*\frac{\partial^4 w(\mathbf{x},t)}{\partial x_2^4}\right]\\
&+\sum_r\sum_{i,j} M_r^{(ij)}\left[\ddot{w}(\mathbf{x},t)+\ddot{z}_r^{(ij)}(t)\right]\\
&\delta(\mathbf{x}-\mathbf{x}^{(ij)}) = F(x_1,x_2,t)e^{-i(k_1x_1+k_2x_2)}\delta(\mathbf{x}-\mathbf{x}^{(ij)}),\\
&M_r^{(ij)}\left[\ddot{w}(\mathbf{x}^{(ij)},t)+\ddot{z}_r^{(ij)}(t)\right] + K_r^{(ij)}z_r^{(ij)}(t)\\
&+K_r^{(ij)(3)}(z_r^{(ij)}(t))^3 = 0,\\
&\text{with}\quad r=1,\dots R,\quad i,j=-\infty,\dots,\infty.
\end{aligned} \tag{B1}$$

Similar to Eq. (13), the harmonic excitation force with amplitude f and frequency $\omega^{(e)}$ at $\mathbf{x}^{(ij)}$ reads:

$$\begin{aligned}
&F(x_1,x_2,t)\delta(\mathbf{x}-\mathbf{x}^{(ij)})\\
&=\sum_m\sum_n F_{mn}(t)e^{-iG_1^{(m)}x_1}e^{-iG_2^{(n)}x_2}\delta(\mathbf{x}-\mathbf{x}^{(ij)})\\
&=\frac{f\cos(\omega^{(e)}t)}{a^2}e^{-i(k_1x_1+k_2x_2)}\\
&\sum_m\sum_n e^{-iG_1^{(m)}x_1}e^{-iG_2^{(n)}x_2},
\end{aligned} \tag{B2}$$

where c represents the damping of the plate on each harmonic component. Let $F_{mn}^* = \frac{f}{a^2}\cos(\omega^{(e)}t)$, one obtains

$$\begin{aligned}
&e^{-i(k_1x_1+k_2x_2)}\sum_n\sum_m\Big\{\rho^\star h\ddot{W}_{mn}(t)+c\dot{W}_{mn}(t)\\
&+\kappa W_{mn}(t)+\sum_r M_r^*[\ddot{w}_0(t)+\ddot{z}_{0r}(t)]-F_{mn}^*\Big\}\\
&e^{-i(G_1^{(m)}x_1+G_2^{(n)}x_2)}=0.
\end{aligned} \tag{B3}$$

To satisfy the equation of motion at any (x_1,x_2), we prescribe in the same spirit of the harmonic balance method that each harmonic term vanishes; that is,

$$\begin{aligned}
&\rho^\star h\ddot{W}_{mn}(t)+c\dot{W}_{mn}(t)+\kappa W_{mn}(t)\\
&+\sum_{r=1}^{R}\left[M_r^*\left(\sum_{m=-N}^{N}\sum_{n=-N}^{N}\ddot{W}_{mn}(t)+\ddot{z}_{0r}(t)\right)\right]\\
&=F_{mn}^*,\quad m,n=-N,\dots,N,\\
&M_r^*\left(\sum_{m=-N}^{N}\sum_{n=-N}^{N}\ddot{W}_{mn}(t)+\ddot{z}_{0r}(t)\right)\\
&+K_rz_{0r}(t)+K_r^{(3)}(z_{0r}(t))^3=0,\quad r=1,\dots,R,
\end{aligned} \tag{B4}$$

where N is the number of retained harmonics. Upon introducing the nondimensional variables and parameters in Eq. (21), one can obtain Eq. (37).

References

1. Laude, V.: Phononic Crystals. De Gruyter, Berlin (2015)
2. Deymier, P.A.: Acoustic Metamaterials and Phononic Crystals. Springer, Berlin (2015)
3. Ma, G., Sheng, P.: Acoustic metamaterials: From local resonances to broad horizons. Sci. Adv. **2**, 1501595 (2016)
4. Hussein, M.I., Leamy, M.J., Ruzzene, M.: Dynamics of phononic materials and structures: historical origins, recent progress, and future outlook. Appl. Mech. Rev. **66**(4), 040802 (2014)
5. Lu, M.-H., Feng, L., Chen, Y.-F.: Phononic crystals and acoustic metamaterials. Mater. Today **12**(12), 34–42 (2009)
6. Liu, L., Sridhar, A., Geers, M., Kouznetsova, V.: Computational homogenization of locally resonant acoustic metamaterial panels towards enriched continuum beam/shell structures. Comput. Methods Appl. Mech. Eng. **387**, 114161 (2021)
7. Jung, J., Goo, S., Wang, S.: Investigation of flexural wave band gaps in a locally resonant metamaterial with plate-like resonators. Wave Motion **93**, 102492 (2020)
8. Lim, C., Li, J.T., Zhao, Z., et al.: Lightweight architected lattice phononic crystals with broadband and multiband vibration mitigation characteristics. Extreme Mech. Lett. **41**, 100994 (2020)

9. Chaunsali, R., Chen, C.-W., Yang, J.: Subwavelength and directional control of flexural waves in zone-folding induced topological plates. Phys. Rev. B **97**(5), 054307 (2018)
10. Guo, W., Yang, Z., Feng, Q., Dai, C., Yang, J., Lei, X.: A new method for band gap analysis of periodic structures using virtual spring model and energy functional variational principle. Mech. Syst. Signal Process. **168**, 108634 (2022)
11. Bacigalupo, A., Gambarotta, L.: Simplified modelling of chiral lattice materials with local resonators. Int. J. Solids Struct. **83**, 126–141 (2016)
12. Comi, C., Driemeier, L.: Wave propagation in cellular locally resonant metamaterials. Lat. Am. J. Solids Struct. **15**, e38 (2018)
13. Matlack, K.H., Bauhofer, A., Krödel, S., Palermo, A., Daraio, C.: Composite 3d-printed metastructures for low-frequency and broadband vibration absorption. Proc. Natl. Acad. Sci. **113**(30), 8386–8390 (2016)
14. Wang, Q., Li, J., Zhang, Y., Xue, Y., Li, F.: Bandgap properties in metamaterial sandwich plate with periodically embedded plate-type resonators. Mech. Syst. Signal Process. **151**, 107375 (2021)
15. Griffina, P., Nagel, P., Koshel, R.D.: The plane-wave expansion method. J. Math. Phys. **15**, 1913–1917 (1974)
16. Poggetto, V.F.D., Serpa, A.L.: Elastic wave band gaps in a three-dimensional periodic metamaterial using the plane wave expansion method. Int. J. Mech. Sci. **184**, 105841 (2020)
17. Dal Poggetto, V.F., Serpa, A.L.: Flexural wave band gaps in a ternary periodic metamaterial plate using the plane wave expansion method. J. Sound Vib. **495**, 115909 (2021)
18. Miranda, E.J.P., Nobrega, E.D., Ferreira, A.H.R., Dos Santos, J.M.C.: Flexural wave band gaps in a multi-resonator elastic metamaterial plate using kirchhoff-love theory. Mech. Syst. Signal Process. **116**, 480–504 (2019)
19. Miranda, E.J.P., Nobrega, E.D., Rodrigues, S.F., Aranas, C., Dos Santos, J.M.C.: Wave attenuation in elastic metamaterial thick plates: analytical, numerical and experimental investigations. Int. J. Solids Struct. **204–205**, 138–152 (2020)
20. Murer, M., Guruva, S.K., Formica, G., Lacarbonara, W.: A multi-bandgap metamaterial with multi-frequency resonators. J. Compos. Mater. **57**(4), 783–804 (2023)
21. Gong, C., Fang, X., Cheng, L.: Band degeneration and evolution in nonlinear triatomic metamaterials. Nonlinear Dyn. **111**, 97–112 (2023)
22. Zhou, W., Wang, Y.-Z.: Metamaterial robot driven by nonlinear elastic waves with stop band and nonreciprocal crawling. Nonlinear Dyn. **112**, 5825–5845 (2024)
23. Fan, X., Mao, X., Dong, Y., Liu, H., Shao, M., Wang, L.: Tunable bandgaps of a metamaterial beam with nonlinear magnetic resonators. Nonlinear Dyn. **112**, 9743–9765 (2024)
24. Nayfeh, A.H., Mook, D.T.: Nonlinear Oscillations. John, New-York (1979)
25. Fronk, M.D., Fang, L., Packo, P., Leamy, M.J.: Elastic wave propagation in weakly nonlinear media and metamaterials: a review of recent developments. Nonlinear Dyn. **111**, 10709–10741 (2023)
26. Fang, L., Leamy, M.J.: A perturbation approach for predicting wave propagation at the spatial interface of linear and nonlinear one-dimensional lattice structures. Nonlinear Dyn. **112**, 5015–5036 (2024)
27. Yu, X., Wang, L.: Nonlinear dynamics of coupled waves in kresling origami metamaterials. J. Sound Vib. **577**, 118263 (2024)
28. Fang, X., Wen, J., Cheng, L., Yu, D., Zhang, H., Gumbsch, P.: Programmable gear-based mechanical metamaterials. Nat. Mater. **21**, 869–876 (2022)
29. Xue, Y., Li, J., Wang, Y., Song, Z., Krushynska, A.O.: Widely tunable magnetorheological metamaterials with nonlinear amplification mechanism. Int. J. Mech. Sci. **264**, 108830 (2024)
30. Jiang, T., Han, Q., Li, C.: Topologically tunable local-resonant origami metamaterials for wave transmission and impact mitigation. J. Sound Vib. **548**, 117548 (2023)
31. Fang, X., Wen, J., Bonello, B., Yin, J., Yu, D.: Ultra-low and ultra-broad-band nonlinear acoustic metamaterials. Nat. Commun. **8**, 1288 (2017)
32. Zhao, J., Zhou, H., Yi, K., Kovacic, I., Zhu, R.: Ultra-broad bandgap induced by hybrid hardening and softening nonlinearity in metastructure. Nonlinear Dyn. **111**, 17687–17707 (2023)
33. Shen, Y., Lacarbonara, W.: Nonlinear dispersion properties of metamaterial beams hosting nonlinear resonators and stop band optimization. Mech. Syst. Signal Process. **187**, 109920 (2023)
34. Shen, Y., Lacarbonara, W.: Wave propagation and multi-stopband behavior of metamaterial lattices with nonlinear locally resonant membranes. Int. J. Non-Linear Mech. **161**, 104671 (2024)
35. Casalotti, A., El-Borgia, S., Lacarbonara, W.: Metamaterial beam with embedded nonlinear vibration absorbers. Int. J. Non-Linear Mech. **98**, 32–42 (2018)
36. Shen, Y., Lacarbonara, W.: Nonlinearity-enhanced wave stop bands in honeycombs embedding spider web-like resonators. J. Sound Vib. **562**, 117821 (2023)
37. Shen, Y., Lacarbonara, W.: Optimal resonator damping for wave propagation control in mechanical metamaterials. Mech. Res. Commun. **130**, 104124 (2023)
38. Gibson, L.J., Ashby, M.F.: Cellular Solids: Structure and Properties. In: Cambridge Solid State Science Series, 2nd edn. Cambridge University Press, Cambridge (1997)
39. Nemeth, M.P.: A treatise on equivalent-plate stiffnesses for stiffened laminated-composite plates and plate-like lattices. Technical report (2011)
40. Lacarbonara, W.: Nonlinear Structural Mechanics. Theory, Dynamical Phenomena and Modeling, 1st edn. Springer, New York (2013)